Nano Research

ISSN 1998-0124 CN 11-5974/O4
https://doi.org/10.1007/s12274-024-6871-3

Research Article

Electrolyte design for Li-conductive solid-electrolyte interphase enabling benchmark performance for all-solid-state lithium-metal batteries

Cailing Fan[1], Niaz Ahmad[1] (✉), Tinglu Song[3], Chaoyuan Zeng[1] (✉), Xiaoxiao Liang[1], Qinxi Dong[1] (✉), and Wen Yang[2] (✉)

[1] *School of Chemistry and Chemical Engineering, Key Laboratory of Ministry of Education for Advanced Materials in Tropical Island Resources, Collaborative Innovation Center of Ecological Civilization, Hainan University, Haikou 570228, China*
[2] *Key Laboratory of Cluster Science of Ministry of Education, Beijing Key Laboratory of Photoelectronic/Electrophotonic Conversion Materials, School of Chemistry and Chemical Engineering, Beijing Institute of Technology, Beijing 100081, China*
[3] *Experimental Center of Advanced Materials, School of Materials Science and Engineering, Beijing Institute of Technology, Beijing 100081, China*

Received: 24 April 2024 / **Revised:** 14 June 2024 / **Accepted:** 8 July 2024

ABSTRACT

Sulfide-based solid-state electrolytes (SSEs) with high Li^+ conductivity (σ_{Li^+}) and trifling grain boundaries have great potential for all-solid-state lithium-metal batteries (ASSLMBs). Nonetheless, the *in-situ* development of mixed ionic-electronic conducting solid-electrolyte interphase (SEI) at sulfide electrolyte/Li-metal anode interface induces uneven Li electrodeposition, which causes Li-dendrites and void formation, significantly severely deteriorating ASSLMBs. Herein, we propose a dual anionic, e.g., F and N, doping strategy to $Li_7P_3S_{11}$, tuning its composition in conjunction with the chemistry of SEI. Therefore, novel $Li_{6.58}P_{2.76}N_{0.03}S_{10.12}F_{0.05}$ glass-ceramic electrolyte ($Li_7P_3S_{11}$-5LiF-3Li_3N-gce) achieved superior ionic (4.33 mS·cm^{-1}) and lowest electronic conductivity of 4.33 × 10^{-10} S·cm^{-1} and thus, offered superior critical current density of 0.90 mA·cm^{-2} (2.5 times > $Li_7P_3S_{11}$) at room temperature (RT). Notably, Li//Li cell with $Li_{6.58}P_{2.76}N_{0.03}S_{10.12}F_{0.05}$-gce cycled stably over 1000 and 600 h at 0.2 and 0.3 mA·cm^{-2} credited to robust and highly conductive SEI (*in-situ*) enriched with LiF and Li_3N species. Li_3N's wettability renders SEI to be highly Li^+ conductive, ensures an intimate interfacial contact, blocks reductive reactions, prevents Li-dendrites and facilitates fast Li^+ kinetics. Consequently, $LiNi_{0.8}Co_{0.15}Al_{0.05}O_2$ (NCA)/$Li_{6.58}P_{2.76}N_{0.03}S_{10.12}F_{0.05}$-gce/Li cell exhibited an outstanding first reversible capacity of 200.8/240.1 mAh·g^{-1} with 83.67% Coulombic efficiency, retained 85.11% of its original reversible capacity at 0.3 mA·cm^{-2} over 165 cycles at RT.

KEYWORDS

$Li_{6.58}P_{2.76}N_{0.03}S_{10.12}F_{0.05}$-glass-ceramic electrolyte (gce), low electronic conductivity, highly Li^+ conductive solid-electrolyte interphase (SEI), Li-dendrites and void suppression, all-solid-state Li-metal batteries

1 Introduction

In the 1970s, Stanley Whittingham developed a rechargeable lithium-metal battery (LMB) using titanium disulfide (TiS_2) single crystal cathode, liquid electrolyte (LE) ($LiPF_6$ dissolved in propylene carbonate) and lithium-metal anode [1], wherein Li^+ intercalated and de-intercalated in discharge and charge process accordingly: $xLi + TiS_2 \leftrightarrow 2Li_xTiS_2$. Notably, the Li//$TiS_2$ cell delivered a phenomenal high energy density of ~ 480 Wh·kg^{-1}. However, Li-dendrite formation prevented the LMBs from being commercialized as it increased the risk of short circuits, fires and even explosions. Hence, Li^+ intercalation carbonaceous materials (graphite: Li_xC_6) in rechargeable lithium-ion batteries (LIBs) had to replace Li-metal. Yoshino et al. developed an LIB consisting of a graphite anode, $LiCoO_2$ cathode and liquid electrolyte ($LiClO_4$ dissolved in propylene carbonate) proved to be safer than LMBs [2]. However, the safety melioration of LIBs over LMBs comes at the cost of energy density. The energy density of the current state-of-the-art LIBs has hardly reached its limit of ~ 300 Wh·kg^{-1}, which is far from the target (500–700 Wh·kg^{-1}) necessary for the vehicle's electrification [3]. Therefore, new battery chemistries are urgently desired using fire retardant electrolytes with high high-energy cathodes and anodes [4–6].

For next-generation battery technologies, solid-state electrolytes (SSEs) can eliminate life-threatening safety concerns and elevate gravimetric energy density (Wh·kg^{-1}) by coupling with Li-metal anode and high-voltage cathodes [7–9]. Due to their absolute solid-state nature, ASSLMBs' performance is greatly influenced by the speed at which Li^+ can move through the SSEs and the durability and effectiveness of the intimate contact between the SSEs and electrodes during cycling. Among the versatile inorganic solid electrolytes (ISEs), sulfide-based solid electrolytes (SSEs) have decent mechanical strength (Young's moduli: 18 to 25 GPa), negligible grain-boundaries (GBs), unity Li^+ transference number and outstanding Li^+ conductivity (σ_{Li^+}) ~ 1–25 mS·cm^{-1}, which is

Address correspondence to Niaz Ahmad, ahmadniaz@hainanu.edu.cn, mna718@outlook.com; Chaoyuan Zeng, zengchaoyuan@hainanu.edu.cn; Qinxi Dong, dongqinxi@hainanu.edu.cn; Wen Yang, wenyang@bit.edu.cn

comparable to or even beating the liquid electrolytes [8, 10, 11]. Nevertheless, recent theoretical and experimental studies investigated that the abovementioned features are not the only criteria for perfect SSEs. Modern research has identified some significant limitations that prevented their practical implementation: (1) narrow electrochemical stability window (ESW) ~ 1.7–2.31 V [12, 13], (2) negative interface energy with Li-metal anode [14] and (3) higher bulk electronic conductivities [15]. Former two factors correlated to electrochemical reduction by Li-metal trigger irretrievable redox reaction of $PS_4^{3-}/P_2S_7^{4-}$ causes the structural collapse and decomposition of the electrolyte, developing mixed ionic-electronic conducting interphase (MCI) dominated with Li_2S, Li_3P and Li_xP, etc. at the Li/sulfide-based SEs interface. The interphase enriched with electronic conductive species (e.g., Li_3P, $Li_{15}Ge_4$, etc.) drives incessant decomposition of sulfide SEs, leads to uneven Li-stripping and plating, promotes the growth of Li-dendrites, voids and cracks formation and eventually contact loss at the Li/SSE interface, increasing the interfacial resistance and deteriorating the cycle life (Scheme 1) [14, 16–18]. Alongside, higher bulk electronic conductivity (σ_{e^-}: 10^{-9}–10^{-8} S·cm^{-1}) negatively influences critical current density (CCD), which therefore, triggers Li-dendrites inside SSEs, leading to short circuits and battery failure [15].

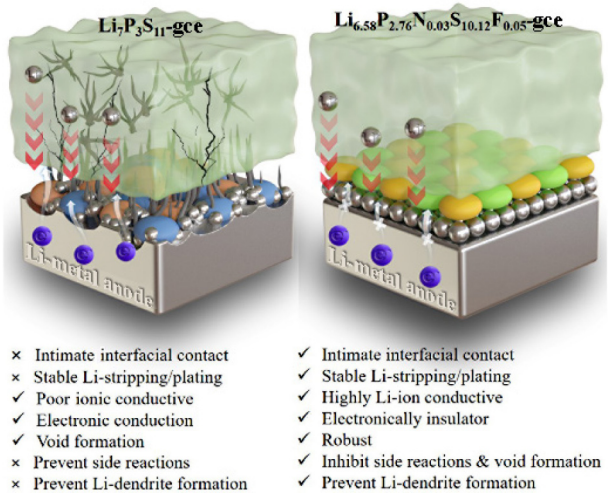

Scheme 1 Illustrating properties of *in-situ* SEI produced between Li/$Li_7P_3S_{11}$-gce and Li/$Li_{6.58}P_{2.76}N_{0.03}S_{10.12}F_{0.05}$-gce.

Electrolyte modifications by pertinent elements, e.g., F, I, N and O [17–20], have proved to be a unique strategy, intrinsically tuning the composition of structural frameworks, which enhances conductive properties and improves their chemical and electrochemical stability against electrodes [19–22]. For instance, incorporating elements, e.g., LiI integrated into Li_3PS_4, results in the development of an *in-situ* solid-electrolyte interphase (SEI) dominated by LiI, suppresses parasitic reactions, enhances CCD (1 mA·cm^{-2}) and ensures homogeneous Li deposition at the interface, which inhibits the formation of Li-dendrites within the electrolyte [23]. Zhao et al. produced $LPSCl_{0.3}F_{0.7}$, wherein F induced a highly fluorinated SEI, effectively intimidated the decomposition reaction and exhibited outstanding stability toward Li-metal during Li stripping/plating operation [24]. Liu et al. studied the influence of nitrogen (N) dopant, generated an *in-situ* SEI, enriched with highly Li^+ conductive Li_3N, promoting Li^+ kinetics across the interface and uniform Li^+ distribution alleviate the formation inside $Li_{6.25}PS_{4.75}N_{0.25}Cl$ [25]. Very recently, Liu et al. regulated the electronic distribution by MgF_2 doping, which has effectively inhibited the redox reactions between Li_6PS_5Cl-MgF_2 and Li-metal and thus, the $LiCoO_2/Li_6PS_5Cl$-MgF_2/Li battery realized remarkable cycling stability (93.3% over 100 cycles at 0.2 °C against 25 °C) [17].

Unquestionably, the composition of the SEI, which in principle, depends on the electrolyte's design, significantly affects the interface stability against Li-metal anodes. Therefore, the SEI (*ex-situ*/*in-situ*) holds the given characteristics: (1) electrochemical stability against Li-metal; (2) electrically insulator but ionically conductive; and (3) high interface energy vs. Li-metal; will not only prevent severe reductive decomposition but also will reduce the formation of Li-dendrite inside the SSE. Accordingly, LiF possesses ultrahigh mechanical strength (e.g., shear modulus of 54.2 GPa), high interface energy versus Li (73.28 meV·Å^{-2}) and the lowest electronic conductivity (σ_{e^-}) effectively stabilizes the SEI layer. However, its low σ_{Li^+} (~ 10^{-9} S·cm^{-1}) causes sluggish Li^+ kinetics across the interphase. Adversely, Li_3N due to its high σ_{Li^+} (~ 10^{-3} S·cm^{-1}) and low σ_{e^-} (< 10^{-12} S·cm^{-1}), greatly prevents the growth of Li-dendrites and accelerates the Li^+ kinetics across the SEI in electrochemical operation [26].

Herein, we propose a dual anionic, e.g., F and N, doping strategy to tune the composition $Li_7P_3S_{11}$ SSE in conjunction with the chemistry of SEI. The successful incorporation of F and N was carried out by high-energy ball-mill technology. The optimized $Li_{6.58}P_{2.76}N_{0.03}S_{10.12}F_{0.05}$-glass-ceramic electrolyte (gce) ($Li_7P_3S_{11}$-5LiF-3Li_3N (7311-5LF-3LN)) presented superior σ_{Li^+} of 4.33 mS·cm^{-1} with the lowest σ_{e^-} of 4.33 × 10^{-10} S·cm^{-1} at room temperature (RT). Accompanied by superior conductive properties, Li//Li symmetric cell with $Li_{6.58}P_{2.76}N_{0.03}S_{10.12}F_{0.05}$-gce showed an ultrastable Li-plating/stripping behavior over 1000 and 600 h at 0.2 and 0.3 mA·cm^{-2} respectively at RT. The outstanding stability of $Li_{6.58}P_{2.76}N_{0.03}S_{10.12}F_{0.05}$-gce toward Li-metal is indexed to highly ionic but electronically insulated SEI, enriched with LiF and Li_3N species confirmed by X-ray photoelectron spectroscopy (XPS) and time-of-flight secondary ion mass spectrometry (ToF-SIMS) analysis. In addition, Li//$LiNi_{0.8}Co_{0.15}Al_{0.05}O_2$ (NCA) full cell with $Li_{6.58}P_{2.76}N_{0.03}S_{10.12}F_{0.05}$-gce delivered an excellent electrochemical performance, e.g., first reversible capacity of 200.8/240.1 mAh·g^{-1} corresponding to 83.67% Coulombic efficiency (CE) and retained 85.11% of its original reversible capacity at 0.3 mA·cm^{-2} over 165 cycles at RT.

2 Experimental section

2.1 Material synthesis

A series of $Li_7P_3S_{11}$-$(x - y)$%(LiF-Li_3N)-gce was achieved via high-energy ball-milling technology (Fritsch, Pulverisette 7, Germany), followed by a heat-treatment route. Accurately weighed amounts of Li_2S (99.9%; Alfa Aesar), P_2S_5 (99%, P ≥ 27%, Macklin), LiF (99.9%; Alfa Aesar) and Li_3N (99.9%; Alfa Aesar) was packed into zirconia pots (volume: 45 mL) filled with argon-gas and five zirconia balls (diameter: 4 mm). Solid-state reaction (SSR) was performed for 50 h at 510 rpm. The heat of the SSR reaction was exhausted by breaking off the milling operation for a suitable time. Thereafter, the superionic conductive phase was nucleated by heating the as-designed amorphous specimens to temperatures between 240 and 290 °C for 4 h. All the steps were conducted within the glovebox (H_2O and O_2 < 0.1 ppm).

2.2 Structural characterization

X-ray diffraction (XRD) was evaluated via a diffractometer (D8 Advance Bruker, Germany with copper Kα radiation (λ = 1.54178 Å at 45 kV and 40 mA from 2θ = 10°–60° at 5 °·min^{-1}. Raman spectra were generated by Renishaw-2000 Raman spectrometer using an incident laser beam at 532 nm. XPS spectra were developed by XPS (ESCALAB-250Xi) with Al Kα source (1486.6 eV, 50 W, 15 kV) X-ray. Next, XPS raw data was investigated using XPS Peak software and the binding energies

(BEs) were equated with the standard peak of carbon (C 1s = 284.8 eV). The local structure of phosphorus was determined by solid-state ^{31}P and ^{7}Li magic angle spinning (MAS) NMR by a Bruker Ascend 700 MHz NMR apparatus. The ^{31}P and ^{7}Li chemical shifts were standardized in parts per million (ppm) relatives to ammonium dihydrogen phosphate ($(NH_4)H_2PO_4$ chemical shift: 0.81) and 1 mol·dm^{-3} aqueous solution of lithium chloride. Electrolytes (~ 80 mg) were filled into a 1.9 mm zirconia MAS rotor inside the glovebox (Ar-atmosphere) and revolved at 13,300 Hz. A recycling delay of 30 s was satisfactory for the quantitative spectra of specimens.

2.3 Li-ion conductivity

Li^+ conductivities of $Li_7P_3S_{11}$-(x − y)%(LiF-Li_3N)-gce were determined by the alternating current (AC) impedance at Solartron 1400/1470E multichannel electrochemical workstation. The frequency and amplitude were set from 0.1 Hz–1 MHz and 20 mV respectively. Firstly, ~ 200 mg of $Li_7P_3S_{11}$-(x − y)%(LiF-Li_3N)-gce were cold-pressed to produce a pellet (diameter (Ø): ~ 13 mm, thickness: 0.1 mm), which however, was then sandwiched between a couple of stainless steel (SS) plates working as current collectors to form the symmetric blocking cells. To derive an Arrhenius plot, temperature-related σ_{Li^+} were determined by varying the temperatures from 25–85 °C, with an interval of 10 °C.

2.4 Cell assembly and electrochemical measurements

Li/$Li_7P_3S_{11}$-(x − y)%(LiF-Li_3N)-gce/Li cells were fabricated to determine the compatibility/electrochemical stability towards Li-metal anode. Typically, 150 mg of $Li_7P_3S_{11}$-(x − y)%(LiF-Li_3N)-gce was squeezed at 220 MPa and shaped a pellet (Ø: ~ 13 mm). The as-prepared pellet was then sandwiched between a couple of Li-foils (China Energy Lithium Co., Ltd.) and pressed aginn at ~ 50 MPa for 3–5 min. Galvanostatic Li-stripping/plating experiment was executed at LAND battery testing system (C2001A, Wuhan LAND Electronic Co., Ltd. China) with different current densities and cut-off capacities (J = 0.2 mA·cm^{-2}/0.2 mAh·cm^{-2} and 0.3 mA·cm^{-2}/0.3 mAh·cm^{-2}) at RT. Cyclic voltammetry (CV) of $Li_7P_3S_{11}$-(x − y)%(LiF-Li_3N)-gce was studied by Li/SSE/SSE-25 wt.% carbon cell strategy. Here, 150 mg of $Li_7P_3S_{11}$-(x − y)%(LiF-Li_3N)-gce was pressed under an isostatic pressure of 120 MPa. 10 mg of $Li_7P_3S_{11}$-(x − y)%(LiF-Li_3N)-gce ($Li_7P_3S_{11}$-(x − y)%(LiF-Li_3N)-gce: graphite is 75:25 in wt.%) spread on the surface of pellet and isostatically pressured together at 220 MPa. Finally, Li-metal was fixed on the opposite side of the pellet and sandwiched the three-layered setups between a pair of SS plates. CV was measured by scanning the voltage from 0–5 V at 0.1 mV·s^{-1} at RT.

2.5 $LiNbO_3$ (LNO)@NCA/$Li_7P_3S_{11}$-(x − y)%(LiF-Li_3N)-gce/Li all-solid-state LMBs (ASSLMBs)

Firstly, 150 mg of $Li_7P_3S_{11}$-(x − y)%(LiF-Li_3N)-gce was isostatically pressed at 220 MPa and shaped a pellet of Ø: ~ 13 mm. LNO@NCA composite cathode having an active material of ~ 7.5 mg·cm^{-2} evenly spread on the surface of the pellet and pressed under a pressure of 220 MPa for 3–5 min. At last, Li-metal was placed on the opposite side and squeezed at 120 MPa for 3–5 min. Finally, a 3-layered setup was clamped between a pair of SS current collectors. Galvanostatic charge/discharge operation was executed via the LAND battery test system (C2001A, Wuhan LAND Electronic Co., Ltd., China). The cut-off voltage was selected at 2.8–4.2 V (vs. Li/Li$^+$). All the steps, e.g., cell fabrication and electrochemical testing proceeded inside the glovebox (at O_2 and H_2O < 0.01 ppm).

3 Results and discussion

Powder XRD measurements were executed for the phase identification of dually doped $Li_7P_3S_{11}$-(x − y)%(LiF-Li_3N) glass-ceramic electrolytes (Fig. 1(a)). Note: Optimization of the double dopant was realized in two steps. Step-I: LiF was incorporated into parent $Li_7P_3S_{11}$ corresponding to xLiF = 0 mol%, 5 mol%, 10 mol% and 15 mol%. Interestingly, xLiF = 5 mol% was found to be the best ratio, and thus, the resultant $Li_{6.7}P_{2.85}S_{10.45}F_{0.05}$-gce rendered better σ_{Li^+} and σ_{e^-} accompanied with superior chemical/electrochemical properties (Figs. S1–S3 in the Electronic Supplementary Material (ESM)). Step-II Li_3N was introduced into $Li_7P_3S_{11}$-5LiF and optimized as $y$$Li_3N$ = 3 mol%, 5 mol% and 7 mol%. At x − y = 0, the characteristic diffraction pattern is nearly identical to the metastable conductive phase $Li_7P_3S_{11}$ once heated at 270 °C/4 h, compared to the standard referenced card ICSD: 157654. Notably, at x − y = 5LF-3LN, the diffraction pattern is consistent with the metastable conductive crystalline phase, clarifying that LiF and Li_3N do not affect the basic crystal framework of the $Li_7P_3S_{11}$. Thus, $Li_{6.58}P_{2.76}N_{0.03}S_{10.12}F_{0.05}$-gce ($x$ − y = 5LF-3LN) with a space group $P\,1$ can be believed to be a member of the $Li_7P_3S_{11}$ (LPS) family with essential $P_2S_7^{4-}$ di-tetrahedral and PS_4^{3-} tetrahedral units [27]. However, at x − y = 5LF-5LN, the diffraction pattern deviates from the basic crystal framework and eventually undergoes structural transformation toward Li_3PS_4 (PDF: 76-0973) at x − y = 5LF-7LN with some unknown peaks [24, 28]. It is noticed that the pattern at 2θ = 38.6° and 44.9° could be revealed to the excessive LiF once the F is completely introduced into the $Li_7P_3S_{11}$ [24, 29]. The excessive LiF can fill the interstitial positions, e.g., grain boundaries, cracks and pores, which however, in principle reduce the σ_{e^-} results in enhancing the stiffness and inhibiting the nucleation of Li dendrites inside SSEs [24, 29, 30]. Raman spectra (Fig. 1(b)) depicted that at x − y = 0, the superionic conductive phase is developed fundamentally with two phases, e.g., $P_2S_7^{4-}$ and PS_4^{3-}, respectively [31, 32]. Notably, at x − y = 5LF-3LN, the intensity and corresponding area of PS_4^{3-} is significantly increased compared to $P_2S_7^{4-}$. Furthermore, at x − y = 5LF-7LN, the PS_4^{3-} intensity is further increased and exists solely at x − y = 5LF-7LN. The vanishing of $P_2S_7^{4-}$ indicating the phase transformation toward Li_3PS_4 with an additional and broad peak around ~ 385 cm^{-1} revealed an impure phase $Li_4P_2S_6$ [26, 33]. Furthermore, Raman spectra confirm the F incorporation into $Li_7P_3S_{11}$-gce by a slight red shift for P–S symmetric stretching vibration of PS_4^{3-} (~ 421 cm^{-1}) due to the highest electronegativity of F [34]. Besides, the local atmosphere of Lithium and phosphorus was explored through solid-state nuclear magnetic resonance (SS-NMR) [31, 35, 36]. Figure S4(a) in the ESM demos ^{31}P-MAS-NMR of $Li_7P_3S_{11}$-5LiF-$y$$Li_3N$ (0 mol%, 3 mol%, 5 mol% and 7 mol%). At x − y = 0, resonance signals at 86.3 and 90.2 ppm account for PS_4^{3-} and $P_2S_7^{4-}$ respectively, strongly consistent with the literature [27, 31, 36–38]. However, the $P_2S_7^{4-}$ intensity is higher than PS_4^{3-} tetrahedral [36]. Interestingly, at x − y = 5LF-3LN, the intensity of an isolated PS_4^{3-} tetrahedra increased significantly in sharp contrast to $P_2S_7^{4-}$ without any secondary impure phase. Furthermore, at a high degree of dopant, e.g., at x − y = 5LF-5LN, the signal of $P_2S_7^{4-}$ is reduced to be negligible and eventually vanishes at x − y = 5LF-7LN with an impure $P_2S_6^{4-}$ phase at 105 ppm, confirm the phase transformation toward Li_3PS_4 [24]. Hence, the phase transformation corroborates that the fundamental crystal frameworks of SSEs can accommodate the foreign elements limitedly and the extra dosing can induce a partial or complete phase change [24, 39–41]. Next to this, synchrotron XRD and Raman's spectroscopic studies investigated that gce consists of glassy (PS_4^{3-}, $P_2S_7^{4-}$ and $P_2S_6^{4-}$) and superionic

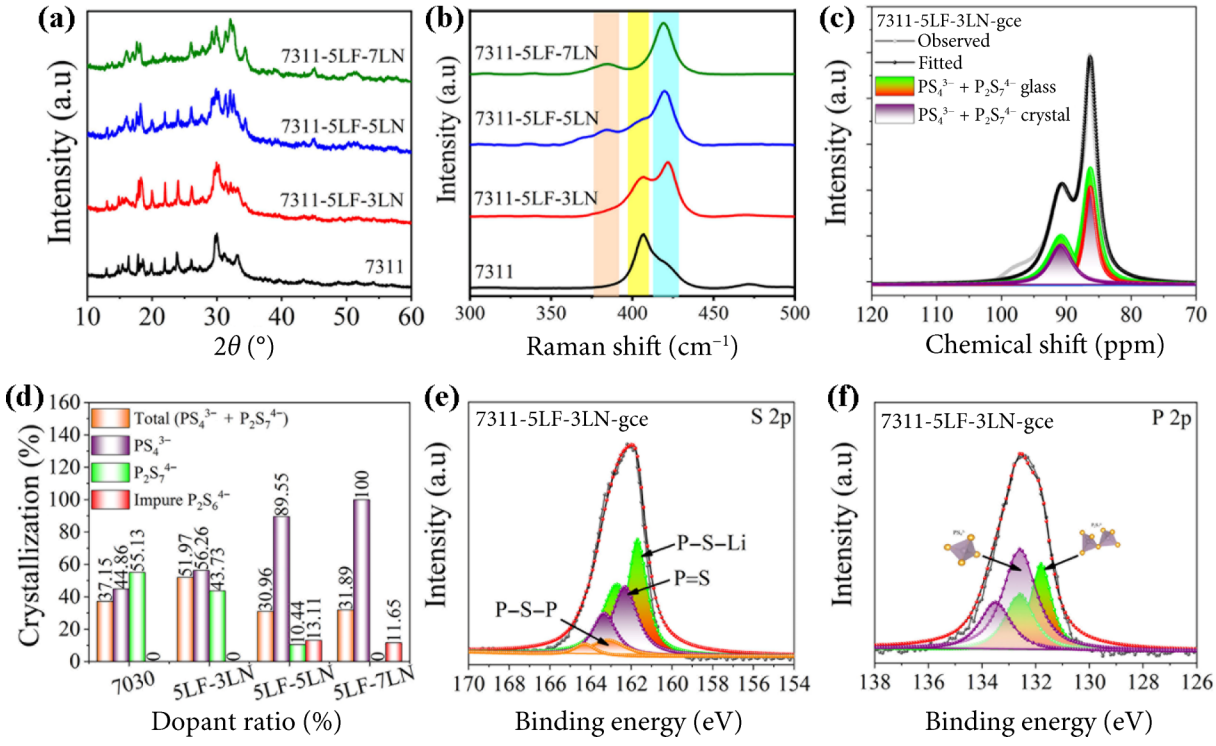

Figure 1 Structural analysis, (a) XRD, (b) Raman spectroscopy $Li_7P_3S_{11}$-($x - y$)%(LiF-Li_3N) glass-ceramic electrolytes, (c) ^{31}P MAS-NMR of $Li_{6.58}P_{2.76}N_{0.03}S_{10.12}F_{0.05}$, (d) degree of crystallization of $Li_7P_3S_{11}$-($x - y$)%(LiF-Li_3N) glass-ceramic electrolytes, (e) XPS S 2p and (f) P 2p spectra of $Li_{6.58}P_{2.76}N_{0.03}S_{10.12}F_{0.05}$.

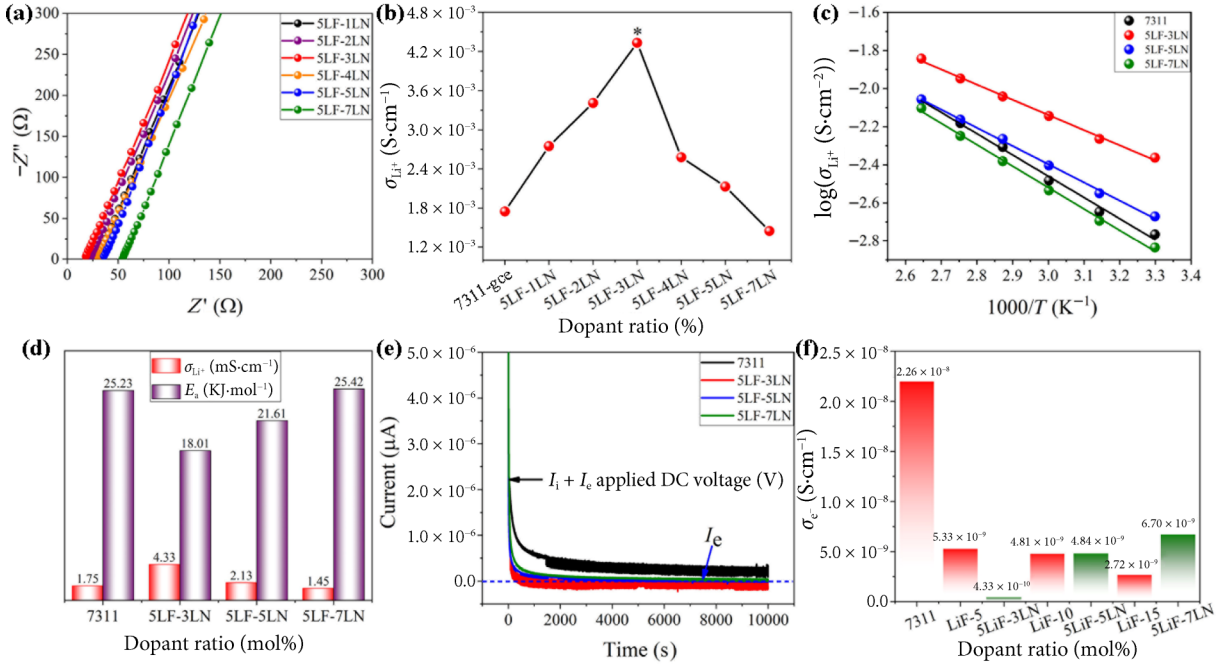

Figure 2 (a) Nyquist plots, (b) σ_{Li^+}, (c) activation energy, (d) comparison of σ_{Li^+} and activation energy, (e) DC polarization and (f) relative electronic conductivities of $Li_7P_3S_{11}$-x%LiF (LiF = 0 mol%, 5 mol%, 10 mol% and 15 mol%) and $Li_7P_3S_{11}$-5LiF-y%Li_3N (Li_3N = 0 mol%, 3 mol%, 5 mol% and 7 mol%) glass-ceramic electrolytes at RT.

conductive crystalline phases (PS_4^{3-} and $P_2S_7^{4-}$) [42, 43]. Accordingly, ^{31}P-MAS-NMR spectra were deconvoluted for detailed structural analysis (Fig. 1(c) and Figs. S4(b)–S4(d) in the ESM). At $x - y = 0$ and $x - y =$ 5LF-3LN, deconvoluted ^{31}P-MAS-NMR spectra consist of four marked peaks. The peaks (green) at 86.3 and 90.2 ppm reflect the glassy phase, while peaks (purple) at 86.3 and 90.2 ppm account for the conductive crystalline phase, respectively. Additionally, at the higher dose of dopants, ^{31}P-MAS-NMR spectra are deconvoluted into five and three peaks, respectively further verifying the phase transition along with the nucleation of impure glassy $P_2S_6^{4-}$ phase. The amount of conductive crystalline phase which, in principle determines the σ_{Li^+} of 7311-($x - y$)%(LF-LN)-gce, can be calculated from Eq. (1) [36]

$$X_c\,(\mathrm{mol\%}) = (\Phi_{PS_4} + \Phi_{P_2S_7})/\Phi_{All} \times 100 \quad (1)$$

Here, X_c stands for crystallization degree, $(\Phi_{PS_4} + \Phi_{P_2S_7})$ unified intensities of Φ_{PS_4} and $\Phi_{P_2S_7}$ in the crystalline phase and Φ_{All} total intensity of all resonances, respectively. The crystallization degree (X_c) and relative change of PS_4 and P_2S_7 conductive phase correspond to the dopant ratio are illustrated in Fig. 1(d). It is notable that the crystallinity of 7311-gce remarkably changed with

dopants and maximized (51.97%) at 5LF-3LN and such a high crystallinity boosts up the σ_{Li^+}. Apart from this, ^{7}Li MAS-NMR was further employed for $Li_7P_3S_{11}$-($x - y$)%(LiF-Li_3N)-gce (Fig. S5 in the ESM), with a narrow peak at 1.7 ppm reflecting the Li site of the conductive phase [26].

XPS elucidated the elemental chemical environment of pristine and LF-LN-doped 7311-gce Figs. 1(e) and 1(f) and Fig. S6 in the ESM. Sebastian et al. studied that 7311-gce fundamentally consists of PS_4^{3-} and $P_2S_7^{4-}$ blocks containing P–S–P, P=S and P–S–Li binding environments [44]. High-resolution S 2p and P 2p XPS spectra of pristine 7311-gce were precisely deconvoluted into peaks P–S–P, P=S, P–S–Li, PS_4^{3-} and $P_2S_7^{4-}$, respectively in agreement with the literature [44–46]. However, once LF-LN dopant was introduced, the peak intensity of P–S–P, principally stemmed from $P_2S_7^{4-}$ decreased and gradually completely vanished 5LF-7LN (Fig. S6(a) in the ESM) also confirming the phase transition and thus consistent with Raman and ^{31}P-MAS-NMR. Likewise, the same trend is observed for P 2p XPS spectra at versatile dopant ratios.

The σ_{Li^+} of 7311-($x - y$)%(LF-LN)-gce was determined by AC impedance. Figures 2(a) and 2(b) represent the Nyquist plots and corresponding σ_{Li^+} of 7311-($x - y$)%(LF-LN)-gce at RT. The σ_{Li^+} of pristine 7311-gce was determined to be 1.75 mS·cm^{-1}. Noticeably, the σ_{Li^+} gradually increases with the dose of dopant, achieving the highest value of 4.33 mS·cm^{-1} versus $x - y$ = 5LF-3LN, and then declines to 1.45 mS·cm^{-1} corresponding to $x - y$ = 5LF-7LN at RT. The drastic decrease in σ_{Li^+} might be indexed to the phase transformation to Li_3PS_4 and the least Li^+ conductive $Li_4P_2S_6$ phase except for low crystallization. At $x - y$ = 5LF-3LN, superior σ_{Li^+} can be attributed to the highest crystallinity (51.97%). Figures 2(c) and 2(d) depict the Arrhenius plots and the relationship of σ_{Li^+} and activation energies of 7311-($x - y$)%(LF-LN)-gce accordingly. It can be seen that 7311-($x - y$)%(5LF-3LN)-gce offers low activation energy E_a of 18.01 kJ·mol^{-1}.

Recently, it has been confirmed that the bulk σ_{e^-} of SSEs is correlated with their CCD [15, 35, 47]. Lithium phosphorus oxynitride (LiPON) for instance, has the lowest bulk electronic conductivity (σ_{e^-}: 10^{-15}–10^{-12} S·cm^{-1}), intrinsically inhibits Li-dendrite's formation corresponding to its highest CCD (> 10 mA·cm^{-2}) [15, 48]. Adversely, high bulk σ_{e^-} (10^{-9}–10^{-7} S·cm^{-1}) of state-of-the-art oxide- and sulfide-based SSEs, e.g., $Li_7La_3Zr_2O_{12}$ and Li_2S-P_2S_5, expediting the nucleation of Li-dendrites ($Li^+ + e^- \rightarrow Li^0$) inside the SSEs [15]. Therefore, direct current (DC) polarization was carried out to evaluate how highly electronegative elements, e.g., F and N, affect the σ_{e^-} of the 7311-($x - y$)%(LF-LN)-gce (Fig. 2(e), testing details in experimental section). The σ_{e^-} of pristine 7311-gce was determined to be 2.16 × 10^{-8} S·cm^{-1} at RT, consistent with the recent literature. In stark contrast, 7311-5LF-3LN-gce demoed the lowest σ_{e^-} of 4.33 × 10^{-10} S·cm^{-1}, which is ~ 2 orders of magnitude lower than that of 7311-gce, minimizing the availability of electrons for Li-ions. Additionally, the σ_{e^-} of the 7311-gce increases and steadily reaches 6.70 × 10^{-9} S·cm^{-1} at higher LF-LN content. The lower σ_{e^-} therefore indeed, can intrinsically restrict the nucleation of Li-dendrites inside the SSE. Moreover, the electro of 7311-($x - y$)%(LF-LN)-gce compared in Fig. 2(f).

Galvanostatic cycling of Li//Li symmetric cells performed at a step-increased current density was used to determine the CCD at RT, demonstrating how the low σ_{e^-} can intrinsically constrain the growth of Li-dendrites. According to Ohm's law ($V = IR$), the voltage is proportional to the current density since the resistance should be nearly constant. A drastic decline in the voltage (V) or area specific resistance (ASR = V/i) attributes the "short-circuit" due to Li-dendrites directly produced inside SSE. Thus, CCD is the highest current density at which voltage drop (short-circuit) is detected, employed to evaluate the capability of Li-dendrite prevention. Accordingly, as presented in Fig. 3(a), the voltage of Li/7311-gce/Li cell irretrievably drops, indicating short-circuit as the current density gradually approaches 0.35 mA·cm^{-2}/0.35 mAh·cm^{-2} at 25 °C. This implies that internal short-circuit could be indexed to the uncontrollable Li-dendrites inside the 7311-gce pellet and MCI (Li_2S and Li_3P) produced by reductive reactions at 7311-gce/Li-metal interface. Unfortunately, MCI with electronic conductive species (Li_3P and $Li_{15}Ge_4$, etc.) not only stimulates Li dendrites' growth but also injects electrons into SSEs thereby resulting in perpetual electrolyte degenerations [14, 16, 17, 49]. In sharp contrast, Li//Li cell with 7311-5LF-3LN-gce (Fig. 3(b)) shows stable Li-stripping/plating up to 0.90 mA·cm^{-2}/0.90 mAh·cm^{-2} at 25 °C (~ 250% improved). Next, as the amount of dopant was further increased $x - y$ = 5LF-5LN and $x - y$ = 5LF-7LN, the CCD gradually declined to 0.4 mA·cm^{-2} (Fig 3(c), Figs. S7(a) and S7(b) in the ESM), which could be blamed on the impure $Li_4P_2S_6$ (σ_{Li^+}: ~ 10^{-11} S·cm^{-1}) phase, subsequently, have adverse effects on the σ_{Li^+} and σ_{e^-} of SSEs (10^{-9} mA·cm^{-2}) [50–53]. Moreover, Fig. 3(c) illustrates that ($x - y$) = 5LF-3LN is an ideal dopant ratio that results in the highest CCD corresponding to its lowest σ_{e^-}. Hereby, the preeminent CCD of 7311-5LF-3LN-gce could be revealed to the given factors; (1) The lowest bulk σ_{e^-} (4.33×10^{-10} mS·cm^{-1}), which in principle, inhibits the direct deposition of Li^0 and thus alleviates the growth Li-dendrites inside SSE; and (2) *In-situ* developed Li^+ SEI not only suppresses reductive reactions but also constrain the nucleation of Li-dendrites produced by uneven electrodeposition of Li^+ at lithium anode. The aforementioned elements work in concert to improve the electrochemical stability/compatibility of SSEs with Li-metal [15, 47, 54–59].

Next, interface stability/compatibility of 7311-($x - y$)%(LF-LN)-gce against Li-metal was investigated by long-term cycling performance through Li//Li symmetric cells under different current densities. Figure S3(a) in the ESM illustrates that Li/7311-gce/Li symmetric cell at J = 0.2 mA·cm^{-2}/0.2 mAh·cm^{-2} cycled with an initial overpotential of ±19 mV. After ~ 70 h, a gradual increase in the overpotential and eventual short-circuiting over 100 h (50 cycles) could be blamed on MCI, void formation and interfacial contact loss [60–62]. The short-circuiting was further confirmed by electrochemical impedance spectroscopy (EIS) (Figs. S8(a) and S8(b) in the ESM). In sharp contrast, Li/7311-5LF-3LN-gce/Li cell tested at J = 0.2 mA·cm^{-2}/0.2 mAh·cm^{-2} (Fig. 3(d)) stripped/plated over 1000 at RT with a flat, reversible and highly stable overpotential (Figs. 3(d1)–3(d3)) presenting 10-times superior cycling performance compared to 7311-gce. Moreover, the cell with 7311-5LF-3LN-gce was further evaluated at J = 0.3 mA·cm^{-2}/0.3 mAh·cm^{-2}, displaying a stable voltage profile for over 675 h (Figs. 3(d1)–3(d3)). The outstanding cycling stability presents the factual interface compatibility between 7311-5LF-3LN-gce and Li-metal anode, as further confirmed by time-resolved EIS measurements (Fig. S9 in the ESM). A minor increase of interfacial resistance might have originated from low σ_{Li^+} of LiF at Li/7311-5LF-3LN-gce interface. The composition of *in-situ* SEI, wherein LiF with high interface energy and low σ_{e^-}, while Li_3N with moderate interface energy and high σ_{Li^+} realize homogenous Li^+ deposition and constraining the growth of Li-dendrites, synergistically increase the interfacial stability between 7311-5LF-3LN-gce and Li-metal. In addition, the performance of Li//Li symmetric cells with higher dopant contents, e.g., 7311-5LF-5LN-gce and 7311-5LF-7LN-gce (Figs. S10(a) and S10(b) in the ESM).

In-situ X-ray computed tomography (X-ray CT) was recently used by Otoyama et al. to demonstrate that the volume at the Li/LPS interface expands ~ 150% when LPS is reduced to Li_2S and Li_3P [63]. Therefore, Li^0 penetrates the LPS layer through the

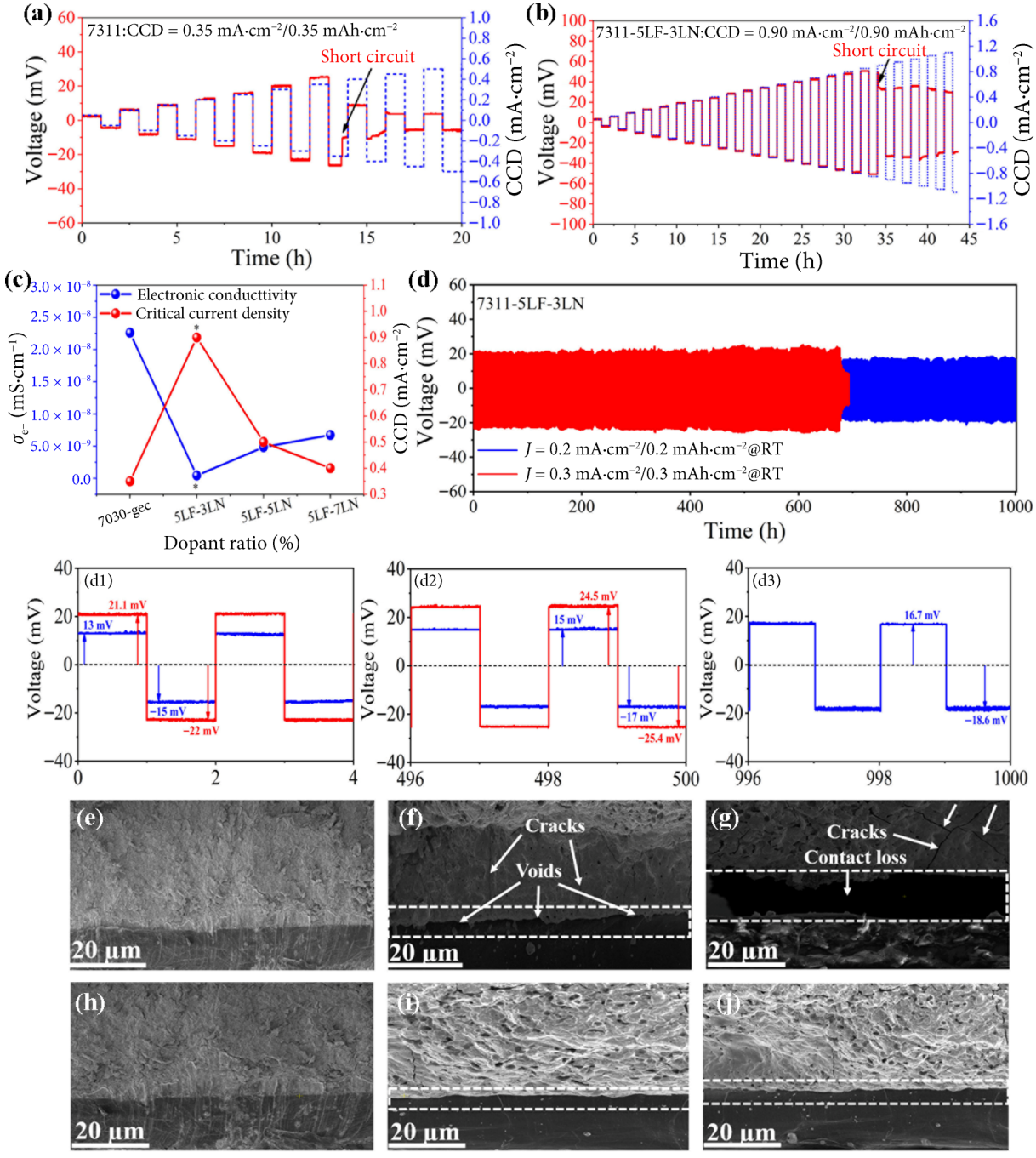

Figure 3 Galvanostatic cycling of the Li-Li cells with step-increased current densities at RT (a) $Li_7P_3S_{11}$, (b) $Li_{6.58}P_{2.76}N_{0.03}S_{10.12}F_{0.05}$, (c) correlation of electronic conductivity and critical current density against different dopant ratio. (d) Galvanostatic long term cycling performance $Li_{6.58}P_{2.76}N_{0.03}S_{10.12}F_{0.05}$ at 0.2 and 0.3 mA·cm^{-2} at RT. Cross-sectional SEM images (e) $Li_7P_3S_{11}$Li and (h) $Li_{6.58}P_{2.76}N_{0.03}S_{10.12}F_{0.05}$ before cycling. (f) and (g) $Li_7P_3S_{11}$ and (i) and (j) Li/$Li_{6.58}P_{2.76}N_{0.03}S_{10.12}F_{0.05}$ after 100 cycles at 0.2 and 0.3 mA·cm^{-2} at RT.

cracks developed in the reduction layers as a result of volume expansion, producing additional reduction layers. According to Ning et al.'s *in-situ* X-ray CT research, cracks are initially formed near the surface of the plated electrode but eventually spread across the electrolyte due to the repeated stripping and plating phenomenon, leading to a short-circuit [64]. Accordingly, *ex-situ* cross-sectional scanning electron microscopy (SEM) was used to visualize the morphological characteristics (interfacial contact and voids) of the interface in Li/7311-gce/Li and Li/7311-5LF-3LN-gce/Li symmetric cells before and after galvanostatic operation. Figures 3(e) and 3(h) project the cross-sectional view of Li/7311-gce and Li/7311-5LF-3LN-gce interface without galvanostatic function, stored for 16 days at RT. Figures 3(i) and 3(j) present that Li/7311-gce/Li cell suffered from cracking, void formation when cycled at J = 0.2 mA·cm^{-2}/0.2 mAh·cm^{-2} and severe contact loss at 0.3 mA·cm^{-2}/0.3 mAh·cm^{-2} over 100 cycles at RT. Cracking, void formation and contact loss are blamed on the decomposition reaction and stress due to the volume change at the Li/electrolyte interface [60, 63–65]. In sharp contrast, Figs. 3(f) and 3(g) elaborate an excellent interfacial contact between 7311-5LF-3LN-gce and Li-metal anode after 100 cycles at J = 0.2 mA·cm^{-2}/0.2 mAh·cm^{-2} and J = 0.3 mA·cm^{-2}/0.3 mAh·cm^{-2}, respectively. The excellent intimate contact could be credited to *in-situ* SEI containing Li_3N, having a solid wetting interaction with Lithium, strengthening the contact and protecting the sulfide from being reduced by Li-metal [56, 59, 66].

Atomic force microscopy (AFM) was conducted to analyze the roughness of Li-metal, retrieved from Li//7311-(x − y)%(LF-LN)-gce//Li cells subjected to galvanostatic cycling at J = 0.2 mA·cm^{-2} and 0.3 mAh·cm^{-2} at RT. Figures 4(a) and 4(b) exhibit topography

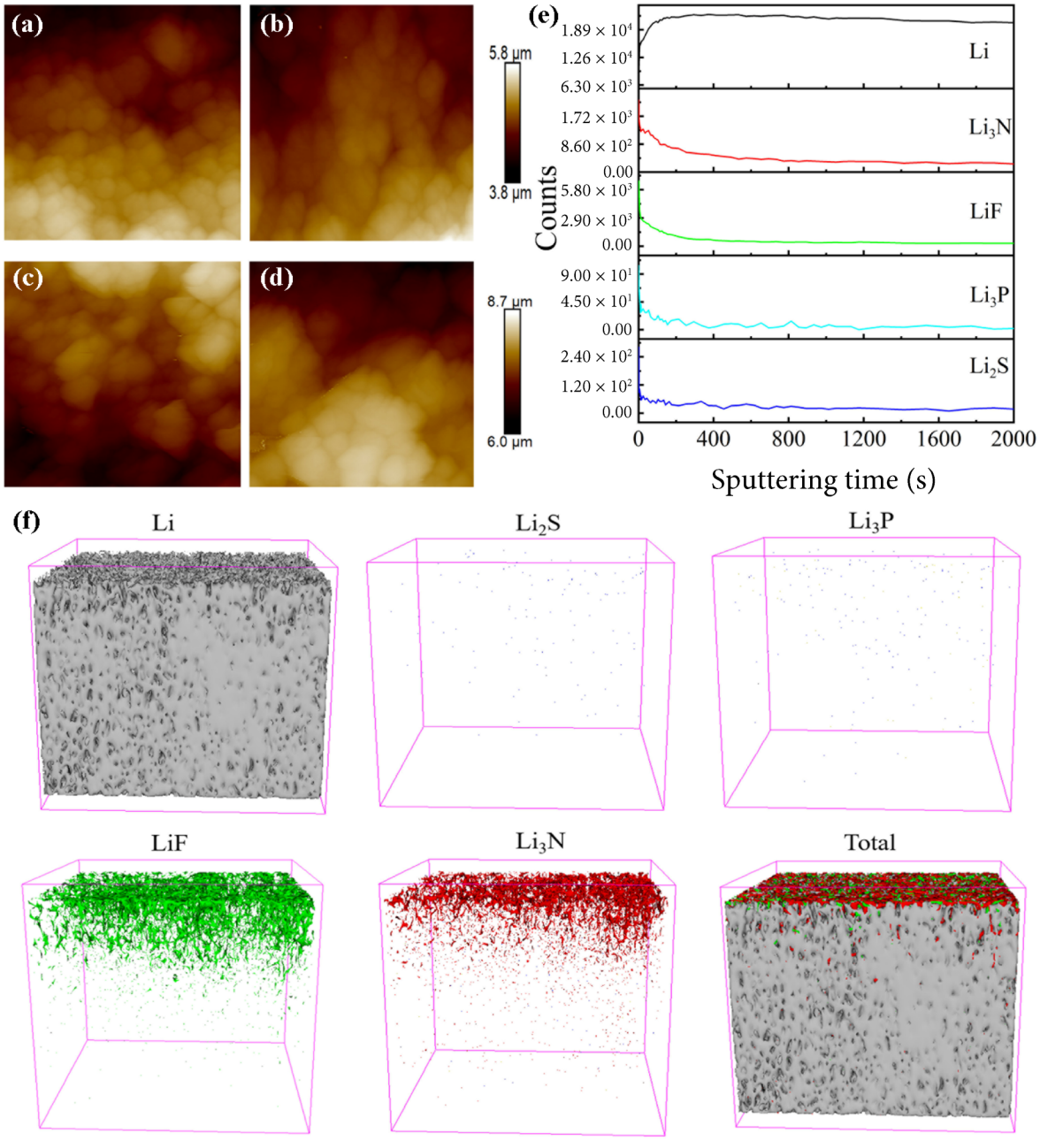

Figure 4 (a) and (b) Morphology of Li-metal anodes retrieved from Li/$Li_{6.58}P_{2.76}N_{0.03}S_{10.12}F_{0.05}$/Li and (c) and (d) Li/$Li_7P_3S_{11}$/Li symmetric cells after 100 cycles at 0.2 and 0.3 mA·cm^{-2} at RT. (e) ToF-SIMS depth profiles of each element on the Li-metal and (f) 3D view images of the sputtered volume corresponding to the depth profiles in (e).

of Li-metal recovered from Li//7311-5LF-3LN-gce//Li cell after 100 cycles, presenting a surface roughness of ~ 167 and 178 nm, respectively. Interestingly, such a low roughness in contrast to pristine Li-foil (Fig. S11 in the ESM) could be credited to the *in-situ* developed SEI enriched with LiF and Li_3N, simultaneously preventing the reduction of electrolyte and uneven Li nucleation results in humongous Li plating/stripping. In sharp contrast, Li-metal retrieved from Li//7311-gce//Li cell present ~ 2-time higher surface roughness (~ 378 and 485 nm) could be revealed to SEI enriched with Li_2S (insulated) and Li_3P (highly electronic conductive) species which provide room for an uneven site of Li plating/stripping (Figs. 4(c) and 4(d)).

ToF-SIMS was executed to identify the chemical compositions of *in-situ* SEI developed on the surface of Li-metal after galvanostatic testing. With Cs^+-ion sputtering, ToF-SIMS depth profiles are shown in Fig. 4(e). The intensity of Li increases with the sputtering up to 500 s and remains stable until 2000 s, suggesting the detection depth is achieving the surface of pure Li-metal. Adversely, the count intensity of LiF and Li_3N is significantly high on the surface layer, decreased gradually up to 800 s, and finally stabilized. However, in sharp contrast, the intensity of Li_2S and Li_3P ~ 2 orders of magnitude lower on the surface layer declined sharply in the first 200 s and got steady later. The results of the depth profiles confirm that SEI is enriched with Li^+ conductive, thermodynamically LiF and Li_3N species. Moreover, a three-dimensional (3D) illustration for the depth profiling can further directly visualize the chemistry of *in-situ* SEI dominated with homogeneously mixed LiF and Li_3N species (Fig. 4(f)).

The *ex-situ* XPS analysis further confirmed the prevention of the reductive interfacial reactions at the Li/SSE interface. Figure 5(a) compared the S 2p XPS spectra of Li/7311 and Li/7311-5LF-3LN-gce interface after galvanostatic cycling. For the Li/7311-gce interface, a pronounced peak at 160.2 eV indexed to the Li_2S. Furthermore, P 2p XPS spectra (Fig. 5(b)) display a distinct peak at 126 eV originating from Li_3P. In sharp contrast, 7311-5LF-3LN-

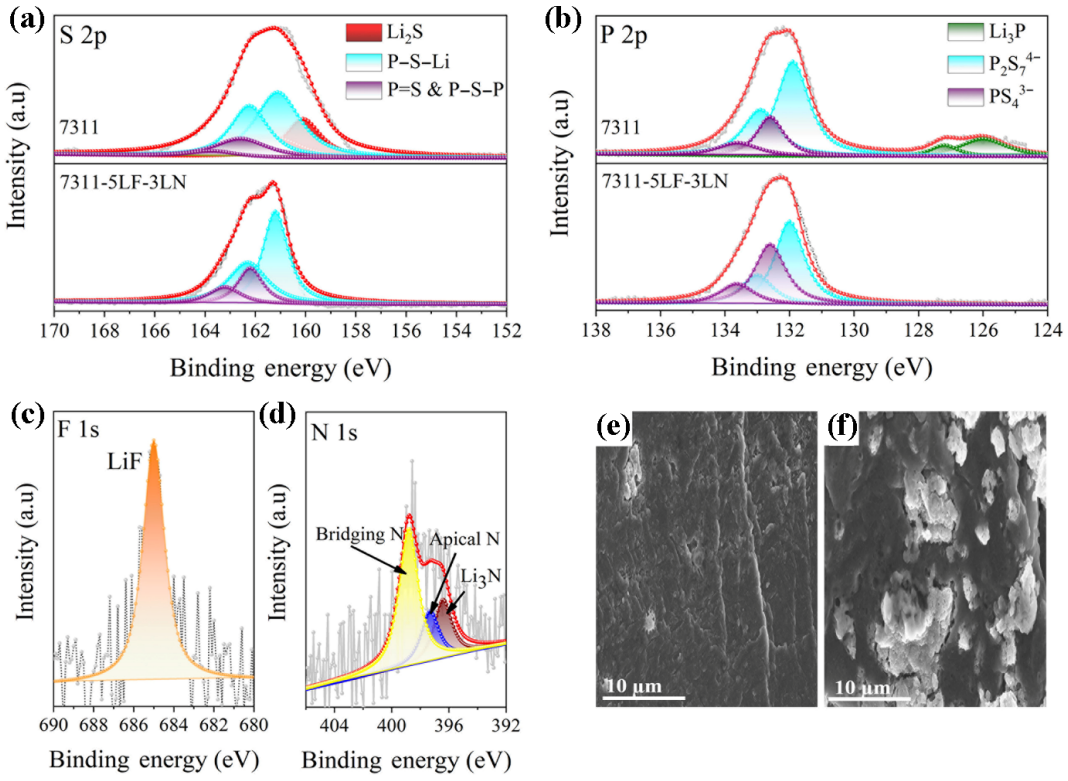

Figure 5 Analysis of interfacial reaction and products. (a) S 2p, (b) P 2p XPS spectra of Li/7311-gce and Li/7311-5LF-3LN-gce after cycling. (c) F 1s and (d) N 1s XPS spectra of Li/7311-5LF-3LN-gce after cycling. (e) and (f) SEM images of Li-metal surface recovered from the Li//Li cells integrated with 7311-5LF-3LN-gce and 7311-gce.

gce effectively suppressed the reduction of S and phosphorous at the interface. Besides, F 1s and N 1s XPS spectra (Figs. 5(c) and 5(d)) corroborate the formation of LiF (~ 684.7 eV) and Li_3N (~ 398 eV) at Li/7311-5LF-3LN-gce interface [14, 67, 68]. In Figs. 5(e) and 5(f), SEM images present Li-metal surface morphology cycled against 7311-5LF-3LN-gce and 731-gce, respectively. The surface of Li-metal retrieved from 7311-5LF-3LN-gce is very smooth without apparent defects. Adversely, the character of Li-metal retrieved from 7311-gce is essentially rough and isolated Li-sulfide agglomeration could be blamed for severe side reactions at the interface (Figs. 4(c) and 4(d)).

CV was performed (Fig. S12 in the ESM) to experimentally evaluate the factual ESW of $Li_7P_3S_{11}$ and $Li_{6.58}P_{2.76}N_{0.03}S_{10.12}F_{0.05}$-gce. In this regard, Li/SSE/SSE-carbon half-cells were assembled and swept from 0–5 V at 0.1 mV·s^{-1} [13, 25]. Hither, a large amount (25 wt.%) of carbon (graphite) was blended with the respective SSEs to form an electrode, which in principle simultaneously increases the σ_{e^-} and kinetics of the decomposition reaction on the account of the facile electronic conduction [13]. It is noticed that the oxidation process of $Li_{6.58}P_{2.76}N_{0.03}S_{10.12}F_{0.05}$ sets out at ~ 2.3 V, consistent with the phase equilibria revealed by the oxidation potential of S and P_2S_5 [12, 69]. However, on the other hand, the reduction process sets out at ~ 1.71 V, indexed to the lithiation process standing for Li_3P and Li_2S [12, 69]. Noticeably, smaller redox currents versus $Li_{6.58}P_{2.76}N_{0.03}S_{10.12}F_{0.05}$ attributed to the superior electrochemical stability against oxidation and reduction compared to pristine 7311. The results indicate that the "true" ESW of $Li_{6.58}P_{2.76}N_{0.03}S_{10.12}F_{0.05}$-gce "1.71–2.31 V" fundamentally, governed by the redox reactions of S and P, which therefore indeed can be tuned by foreign elements agree well with the recently reported (theoretically and experimentally) literature [70, 71].

Based upon the excellent compatibility/electrochemical stability versus Li-metal in Li//Li symmetric cells, the applicability of 7311-(x – y)%(LF-LN)-gce was further evaluated in ASSLMBs at RT. In ASSLMBs, 7311-(x – y)%(LF-LN)-gce were sandwiched between LNO@NCA cathode and bare Li-metal anode, galvanostatically cycled at 0.3 mA·cm^{-2} from 2.8–4.2 V (vs. Li/Li$^+$) at RT (Fig. 6(a), schematic diagam of ASSLMBs). The loading amount of NCA active cathode material was 8.50 mg·cm^{-2}. Figure 6(b), shows the charge–discharge voltage profile of LNO@NCA//Li cell assembled by 7311-gce. The cell delivered an initial reversible capacity of 185.2/258.8 mAh·g^{-1} with η = 71.56% and short-circuited at the 8th cycle. Besides, the impedance of the cell increased from 705 to 1070.5 Ω after short-circuit (Fig. S13(a) in the ESM). In sharp contrast, the LNO@NCA//Li cell with 7311-5LF-3LN-gce presented superior electrochemical performance corresponding to the charge–discharge profile (Fig. 6(c)). The cell delivered first reversible capacity of 200.8/240.1 mAh·g^{-1} corresponding to the 83.83% Coulombic efficiency (η). The initial Coulombic efficiency can be considered as best compared to ASSLMBs paired with bare Li-metal anode. Moreover, the reduced space charge layer phenomenon in the first charged curve corroborating excellent compatibility at 7311-5LF-3LN-gce/LNO@NCA interface led to a reduction in the irreversible capacity loss of 16.32% compared to 28.43% of 7311-gce. Figure 6(d) exhibits excellent long-term performance with a reversible discharge capacity of 171.04 mAh·g^{-1}, corresponding to 85.11% capacity retention and η = 99.53% over 165 cycles. The long-term performance of Li/7311-5LF-3LN-gce/LNO@NCA cell is further compared with state-of-the-art ASSLMBs in Table 1. Furthermore, superior compatibility of 7311-5LF-3LN-gce toward LNO@NCA and Li-metal electrodes was further evidenced by stable time-resolved EIS spectra of Li/7311-5LF-3LN-gce/LNO@NCA cell preserved at an open circuit voltage (OCV) for 16 days (Fig. 6(e)). Nyquist plots of Li/7311-5LF-3LN-gce/LNO@NCA cell before and after testing were further characterized at RT (Fig. 6(f)). The impedance of the cell increased from 50 to 225 Ω over 165 cycles is ~ 4 times lower than that of Li/7311-gce/LNO@NCA cell (Fig. S13(a) in the ESM), confirming that the incorporation of LF-LN mitigates the

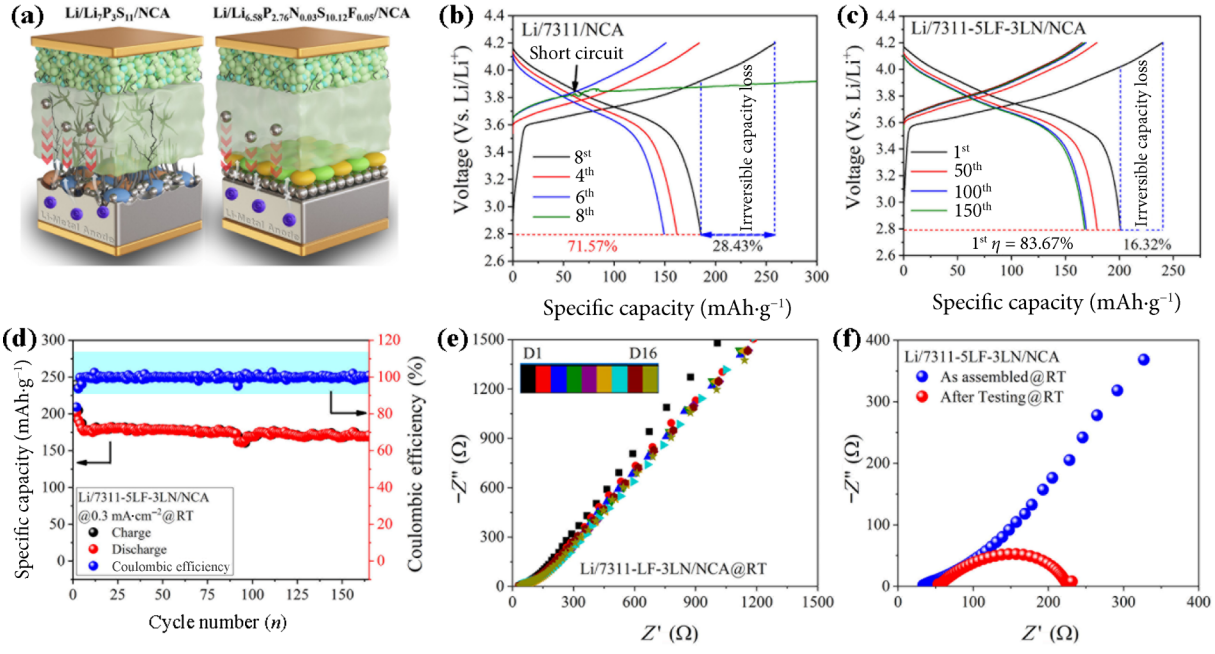

Figure 6 (a) Schematic diagram of Li/7311/NCA and Li/7311-5LF-3LN/NCA cells, (b) and (c) charge–discharge voltage profiles of Li/7311/NCA and Li/7311-5LF-3LN/NCA cells, (d) long-term cycling performance, (e) time-resolved EIS at OCV and (f) EIS spectra of Li/7311-5LF-3LN/NCA cell before and after cycling at RT.

Table 1 Performance summary of sulfide-based all-solid-state Li metal batteries using various oxide base-cathode materials

Battery configuration	Current density	Cycle number/capacity retention)	Active material loading	Test temperature	References
$Li@LPSCl_{0.3}F_{0.7}$//LPSCl//LCO@LNO	0.1 C	50/95%	8.92	RT	[24]
Li@LiF/$Li_7P_3S_{11}$ (HFE)/LCO	0.1 mA·cm^{-2}	50/81.4%	3.6 mg·cm^{-2}	RT	[72]
Li//gc-$Li_{3.2}P_{0.8}Sn_{0.2}S_4$//LCO	0.1 C	60/77%	8.9 mg·cm^{-2}	RT	[73]
Li/$LPSI_{20}Sn$//LGPS//LCO@LNO//LGPS	0.1 C	50/88.5%	—	RT	[74]
Li/$LPSCl_{1.5}$/NCM	0.2 C	100/80.4%	6.24 mg·cm^{-2}	RT	[75]
Li|LiFSI@LPS|LCO	0.3 mA·cm^{-2}	50/—	—	RT	[18]
Li@$LPSI_{1.4}$-gc||LPSC||LCO	0.1 C	50/79.6%	—	RT	[41]
Li/LPSC-MF/$LiCoO_2$	0.1 C	100/92.2%	—	RT	[17]
NCA/$Li_{6.58}P_{2.76}N_{0.03}S_{10.12}F_{0.05}$/Li	0.3 mA·cm^{-2}	165/85.11%	8.50 mg·cm^{-2}	RT	This work

interfacial reaction at both sides which therefore indeed results in superior battery performance.

4 Conclusions

We proposed a dual anionic, F and N doping strategy for $Li_7P_3S_{11}$-gce, which tunes its composition and optimizes the chemistry of SEI, which therefore indeed *in-situ* developed between the electrolyte and Li-metal anode. The newly developed $Li_{6.58}P_{2.76}N_{0.03}S_{10.12}F_{0.05}$-gce achieved superior ionic (4.33 mS·cm^{-1}) and lowest bulk electronic conductivity (4.33 × 10^{-10} S·cm^{-1}; 2 order of magnitude lower than $Li_7P_3S_{11}$) at RT, and hence, presenting higher Li-dendrite suppression capability in-terms of high critical current density of 0.90 mA·cm^{-2}/0.90 mAh·cm^{-2} (2.5 times higher than $Li_7P_3S_{11}$). The $Li_{6.58}P_{2.76}N_{0.03}S_{10.12}F_{0.05}$-gce suppressed drastic side reaction at Li-metal interface due to *in-situ* developed SEI enriched with LiF and Li_3N species confirmed by *ex-situ* XPS and ToF-SIMS technologies. The development of LiF and Li_3N at the Li/electrolyte interface, possessing high interface energy and high Li^+ conductivity, results in suppressing the Li-dendrite generation and their penetration into solid electrolytes. Consequently, $Li_{6.58}P_{2.76}N_{0.03}S_{10.12}F_{0.05}$-gce in Li//Li cell cycled stably over 1000 and 600 h at 0.2 and 0.3 mA·cm^{-2}/mAh·cm^{-2} at RT, significantly superior over $Li_7P_3S_{11}$-base solid electrolytes. Furthermore, NCA//Li full cell with $Li_{6.58}P_{2.76}N_{0.03}S_{10.12}F_{0.05}$-gce delivered an outstanding reversible capacity of 171.04 mAh·g^{-1} over 165 cycles with 85.11% retention at RT.

Acknowledgements

The National Natural Science Foundation of China (Nos. 21203008, 21975025, 12274025 and 22372008), Hainan Province Science and Technology Special Fund (Nos. ZDYF2021SHFZ232 and ZDYF2023GXJS022), Hainan Province Postdoctoral Science Foundation (No. 300333) supported this work.

Electronic Supplementary Material: Supplementary material (critical current density of $Li_7P_3S_{11}$-*x*%LiF, Cyclic performance of Li//Li symmetric cells with $Li_7P_3S_{11}$-*x*%LiF, ^{31}P MAS-NMR: (a) $Li_7P_3S_{11}$-(*x* − *y*)%(LiF-Li_3N), ^7Li MAS-NMR of $Li_7P_3S_{11}$-(*x* − *y*)%(LiF-Li_3N), XPS spectra of $Li_7P_3S_{11}$-(*x* − *y*)%(LiF-Li_3N), Impedance plots, Rest time-resolved EIS profiles, Cycling performance of Li//Li symmetric cells, Topography of pristine Li-metal without cycling in Li//Li cell, cyclic voltammetry and EIS spectra Li/7311/NCA cell before and after cycling at RT and b) time-resolved EIS spectra of Li/7311/NCA cell at OCV at RT) is available in the online version of this article at https://doi.org/10.1007/s12274-024-6871-3.

References

[1] Whittingham, M. S. Electrical energy storage and intercalation chemistry. *Science* **1976**, *192*, 1126–1127.

[2] Yoshino, A. The birth of the lithium-ion battery. *Angew. Chem., Int. Ed.* **2012**, *51*, 5798–5800.

[3] Wang, A. P.; Kadam, S.; Li, H.; Shi, S. Q.; Qi, Y. Review on modeling of the anode solid electrolyte interphase (SEI) for lithium-ion batteries. *npj Comput. Mater.* **2018**, *4*, 15.

[4] Zhang, X. L.; Tang, Y. B.; Zhang, F.; Lee, C. S. A novel aluminum-graphite dual-ion battery. *Adv. Energy Mater.* **2016**, *6*, 1502588.

[5] Wang, M.; Jiang, C. L.; Zhang, S. Q.; Song, X. H.; Tang, Y. B.; Cheng, H. M. Reversible calcium alloying enables a practical room-temperature rechargeable calcium-ion battery with a high discharge voltage. *Nat. Chem.* **2018**, *10*, 667–672.

[6] Wang, L.; Lu, J. J.; Li, S. Y.; Xi, F. S.; Tong, Z. Q.; Chen, X. H.; Wei, K. X.; Ma, W. H. Controllable interface engineering for the preparation of high rate silicon anode. *Adv. Funct. Mater.*, in press, DOI: 10.1002/adfm.202403574.

[7] Janek, J.; Zeier, W. G. Challenges in speeding up solid-state battery development. *Nat. Energy* **2023**, *8*, 230–240.

[8] Famprikis, T.; Canepa, P.; Dawson, J. A.; Islam, M. S.; Masquelier, C. Fundamentals of inorganic solid-state electrolytes for batteries. *Nat. Mater.* **2019**, *18*, 1278–1291.

[9] Manthiram, A.; Yu, X. W.; Wang, S. F. Lithium battery chemistries enabled by solid-state electrolytes. *Nat. Rev. Mater.* **2017**, *2*, 16103.

[10] Wu, J. H.; Liu, S. F.; Han, F. D.; Yao, X. Y.; Wang, C. S. Lithium/sulfide all-solid-state batteries using sulfide electrolytes. *Adv. Mater.* **2021**, *33*, 2000751.

[11] Nose, M.; Kato, A.; Sakuda, A.; Hayashi, A.; Tatsumisago, M. Evaluation of mechanical properties of Na_2S–P_2S_5 sulfide glass electrolytes. *J. Mater. Chem. A* **2015**, *3*, 22061–22065.

[12] Zhu, Y. Z.; He, X. F.; Mo, Y. F. Origin of outstanding stability in the lithium solid electrolyte materials: Insights from thermodynamic analyses based on first-principles calculations. *ACS Appl. Mater. Interfaces* **2015**, *7*, 23685–23693.

[13] Han, F. D.; Zhu, Y. Z.; He, X. F.; Mo, Y. F.; Wang, C. S. Electrochemical stability of $Li_{10}GeP_2S_{12}$ and $Li_7La_3Zr_2O_{12}$ solid electrolytes. *Adv. Energy Mater.* **2016**, *6*, 1501590.

[14] Ji, X.; Hou, S.; Wang, P. F.; He, X. Z.; Piao, N.; Chen, J.; Fan, X. L.; Wang, C. S. Solid-state electrolyte design for lithium dendrite suppression. *Adv. Mater.* **2020**, *32*, 2002741.

[15] Han, F. D.; Westover, A. S.; Yue, J.; Fan, X. L.; Wang, F.; Chi, M. F.; Leonard, D. N.; Dudney, N. J.; Wang, H.; Wang, C. S. High electronic conductivity as the origin of lithium dendrite formation within solid electrolytes. *Nat. Energy* **2019**, *4*, 187–196.

[16] Wenzel, S.; Randau, S.; Leichtweiß, T.; Weber, D. A.; Sann, J.; Zeier, W. G.; Janek, J. Direct observation of the interfacial instability of the fast ionic conductor $Li_{10}GeP_2S_{12}$ at the lithium metal anode. *Chem. Mater.* **2016**, *28*, 2400–2407.

[17] Liu, C.; Chen, B. T.; Zhang, T. R.; Zhang, J. C.; Wang, R. Y.; Zheng, J.; Mao, Q. J.; Liu, X. F. Electron redistribution enables redox-resistible Li_6PS_5Cl towards high-performance all-solid-state lithium batteries. *Angew. Chem., Int. Ed.* **2023**, *62*, e202302655.

[18] Fan, X. L.; Ji, X.; Han, F. D.; Yue, J.; Chen, J.; Chen, L.; Deng, T.; Jiang, J. J.; Wang, C. S. Fluorinated solid electrolyte interphase enables highly reversible solid-state Li metal battery. *Sci. Adv.* **2018**, *4*, eaau9245.

[19] Wei, C. C.; Liu, C.; Xiao, Y. J.; Wu, Z. K.; Luo, Q. Y.; Jiang, Z. L.; Wang, Z. Y.; Zhang, L.; Cheng, S. J.; Yu, C. SnF_2-induced multifunctional interface-stabilized $Li_{5.5}PS_{4.5}Cl_{1.5}$-based all-solid-state lithium metal batteries. *Adv. Funct. Mater.* **2024**, *34*, 2314306.

[20] Wei, C. C.; Xiao, Y. J.; Wu, Z. K.; Liu, C.; Luo, Q. Y.; Jiang, Z. L.; Li, L.; Ming, L.; Yang, J.; Cheng, S. J. et al. Construction of LiCl/LiF/LiZn hybrid SEI interface achieving high-performance sulfide-based all-solid-state lithium metal batteries. *Sci. China Chem.* **2024**, *67*, 1990–2001.

[21] Luo, Q. Y.; Ming, L.; Zhang, D.; Wei, C. C.; Wu, Z. K.; Jiang, Z. L.; Liu, C.; Liu, S. Y.; Cao, K. C.; Zhang, L. et al. Constructing Br-doped $Li_{10}SnP_2S_{12}$-based all-solid-state batteries with superior performances. *Energy Mater. Adv.* **2023**, *4*, 0065.

[22] Chen, S.; Yu, C.; Wei, C. C.; Jiang, Z. L.; Zhang, Z. Q.; Peng, L. F.; Cheng, S. J.; Xie, J. Unraveling electrochemical stability and reversible redox of Y-doped Li_2ZrCl_6 solid electrolytes. *Energy Mater. Adv.* **2023**, *4*, 0019.

[23] Han, F. D.; Yue, J.; Zhu, X. Y.; Wang, C. S. Suppressing Li dendrite formation in Li_2S-P_2S_5 solid electrolyte by LiI incorporation. *Adv. Energy Mater.* **2018**, *8*, 1703644.

[24] Zhao, F. P.; Sun, Q.; Yu, C.; Zhang, S. M.; Adair, K.; Wang, S. Z.; Liu, Y. L.; Zhao, Y.; Liang, J. W.; Wang, C. H. et al. Ultrastable anode interface achieved by fluorinating electrolytes for all-solid-state Li metal batteries. *ACS Energy Lett.* **2020**, *5*, 1035–1043.

[25] Liu, Y.; Su, H.; Li, M.; Xiang, J. Y.; Wu, X. Z.; Zhong, Y.; Wang, X. L.; Xia, X. H.; Gu, C. D.; Tu, J. P. *In situ* formation of a Li_3N-rich interface between lithium and argyrodite solid electrolyte enabled by nitrogen doping. *J. Mater. Chem. A* **2021**, *9*, 13531–13539.

[26] Xu, R. C.; Xia, X. H.; Wang, X. L.; Xia, Y.; Tu, J. P. Tailored Li_2S–P_2S_5 glass-ceramic electrolyte by MoS_2 doping, possessing high ionic conductivity for all-solid-state lithium-sulfur batteries. *J. Mater. Chem. A* **2017**, *5*, 2829–2834.

[27] Lv, L.; Ahmad, N.; Zeng, C. Y.; Yu, P. W.; Song, T. L.; Dong, Q. X.; Yang, W. Enhanced air and electrochemical stability of $Li_7P_{2.9}Ge_{0.05}S_{10.75}O_{0.1}$ electrolytes with high ionic conductivity for thiophosphate-based all-solid-state batteries. *ACS Appl. Mater. Interfaces* **2022**, *14*, 39985–39995.

[28] Wang, Z. X.; Jiang, Y.; Wu, J.; Jiang, Y.; Ma, W. C.; Shi, Y. R.; Liu, X. Y.; Zhao, B.; Xu, Y.; Zhang, J. J. Doping effects of metal cation on sulfide solid electrolyte/lithium metal interface. *Nano Energy* **2021**, *84*, 105906.

[29] Arnold, W.; Shreyas, V.; Li, Y.; Koralalage, M. K.; Jasinski, J. B.; Thapa, A.; Sumanasekera, G.; Ngo, A. T.; Narayanan, B.; Wang, H. Synthesis of fluorine-doped lithium argyrodite solid electrolytes for solid-state lithium metal batteries. *ACS Appl. Mater. Interfaces* **2022**, *14*, 11483–11492.

[30] Kaup, K.; Bazak, J. D.; Vajargah, S. H.; Wu, X. H.; Kulisch, J.; Goward, G. R.; Nazar, L. F. A lithium oxythioborosilicate solid electrolyte glass with superionic conductivity. *Adv. Energy Mater.* **2020**, *10*, 1902783.

[31] Ahmad, N.; Zhou, L.; Faheem, M.; Tufail, M. K.; Yang, L.; Chen, R. J.; Zhou, Y. D.; Yang, W. Enhanced air stability and high Li-ion conductivity of $Li_{6.988}P_{2.994}Nb_{0.2}S_{10.934}O_{0.6}$ glass-ceramic electrolyte for all-solid-state lithium-sulfur batteries. *ACS Appl. Mater. Interfaces* **2020**, *12*, 21548–21558.

[32] Zhou, L.; Tufail, M. K.; Liao, Y. Z.; Ahmad, N.; Yu, P. W.; Song, T. L.; Chen, R. J.; Yang, W. Tailored carrier transport path by interpenetrating networks in cathode composite for high performance all-solid-state Li-SeS_2 batteries. *Adv. Fiber Mater.* **2022**, *4*, 487–502.

[33] Zhao, B. S.; Wang, L.; Chen, P.; Liu, S.; Li, G. R.; Xu, N.; Wu, M. T.; Gao, X. P. Congener substitution reinforced $Li_7P_{2.9}Sb_{0.1}S_{10.75}O_{0.25}$ glass-ceramic electrolytes for all-solid-state lithium-sulfur batteries. *ACS Appl. Mater. Interfaces* **2021**, *13*, 34477–34485.

[34] Deiseroth, H. J.; Kong, S. T.; Eckert, H.; Vannahme, J.; Reiner, C.; Zaiß, T.; Schlosser, M. Li_6PS_5X: A class of crystalline Li-rich solids with an unusually high Li^+ mobility. *Angew. Chem.* **2008**, *120*, 767–770.

[35] Ahmad, N.; Sun, S. R.; Yu, P. W.; Yang, W. Design unique air-stable and Li-metal compatible sulfide electrolyte via exploration of anion functional units for all-solid-state lithium-metal batteries. *Adv. Funct. Mater.* **2022**, *32*, 2201528.

[36] Seino, Y.; Nakagawa, M.; Senga, M.; Higuchi, H.; Takada, K.; Sasaki, T. Analysis of the structure and degree of crystallisation of $70Li_2S$–$30P_2S_5$ glass ceramic. *J. Mater. Chem. A* **2015**, *3*, 2756–2761.

[37] Minami, K.; Mizuno, F.; Hayashi, A.; Tatsumisago, M. Structure and properties of the $70Li_2S{\cdot}(30-x)P_2S_5{\cdot}xP_2O_5$ oxysulfide glasses and glass-ceramics. *J. Non-Cryst. Solids* **2008**, *354*, 370–373.

[38] Murakami, M.; Shimoda, K.; Shiotani, S.; Mitsui, A.; Ohara, K.; Onodera, Y.; Arai, H.; Uchimoto, Y.; Ogumi, Z. Dynamical origin of ionic conductivity for $Li_7P_3S_{11}$ metastable crystal as studied by $^{6/7}Li$ and ^{31}P solid-state NMR. *J. Phys. Chem. C* **2015**, *119*, 24248–24254.

[39] Kim, K. H.; Martin, S. W. Structures and properties of oxygen-substituted $Li_{10}SiP_2S_{12-x}O_x$ solid-state electrolytes. *Chem. Mater.* **2019**, *31*, 3984–3991.

[40] Jiang, Z.; Liang, T. B.; Liu, Y.; Zhang, S. Z.; Li, Z. X.; Wang, D. H.; Wang, X. L.; Xia, X. H.; Gu, C. D.; Tu, J. P. Improved ionic conductivity and Li dendrite suppression capability toward $Li_7P_3S_{11}$-based solid electrolytes triggered by Nb and O cosubstitution. *ACS Appl. Mater. Interfaces* **2020**, *12*, 54662–54670.

[41] Liu, Y.; Peng, H. L.; Su, H.; Zhong, Y.; Wang, X. L.; Xia, X. H.; Gu, C. D.; Tu, J. P. Ultrafast synthesis of I-rich lithium argyrodite glass-ceramic electrolyte with high ionic conductivity. *Adv. Mater.* **2022**, *34*, 2107346.

[42] Yamane, H.; Shibata, M.; Shimane, Y.; Junke, T.; Seino, Y.; Adams,

S.; Minami, K.; Hayashi, A.; Tatsumisago, M. Crystal structure of a superionic conductor, $Li_7P_3S_{11}$. *Solid State Ionics* **2007**, *178*, 1163–1167.

[43] Mizuno, F.; Hayashi, A.; Tadanaga, K.; Tatsumisago, M. High lithium ion conducting glass-ceramics in the system Li_2S–P_2S_5. *Solid State Ionics* **2006**, *177*, 2721–2725.

[44] Wenzel, S.; Weber, D. A.; Leichtweiss, T.; Busche, M. R.; Sann, J.; Janek, J. Interphase formation and degradation of charge transfer kinetics between a lithium metal anode and highly crystalline $Li_7P_3S_{11}$ solid electrolyte. *Solid State Ionics* **2016**, *286*, 24–33.

[45] Busche, M. R.; Weber, D. A.; Schneider, Y.; Dietrich, C.; Wenzel, S.; Leichtweiss, T.; Schröder, D.; Zhang, W. B.; Weigand, H.; Walter, D. et al. *In situ* monitoring of fast Li-ion conductor Li7P3S11 crystallization inside a hot-press setup. *Chem. Mater.* **2016**, *28*, 6152–6165.

[46] Zhao, B.; Shi, Y. R.; Wu, J.; Xing, C.; Liu, Y. Q.; Ma, W. C.; Liu, X. Y.; Jiang, Y.; Zhang, J. J. Stabilizing $Li_7P_3S_{11}$/lithium metal anode interface by *in-situ* bifunctional composite layer. *Chem. Eng. J.* **2022**, *429*, 132411.

[47] Lu, Y.; Zhao, C. Z.; Yuan, H.; Cheng, X. B.; Huang, J. Q.; Zhang, Q. Critical current density in solid-state lithium metal batteries: Mechanism, influences, and strategies. *Adv. Funct. Mater.* **2021**, *31*, 2009925.

[48] Put, B.; Vereecken, P. M.; Meersschaut, J.; Sepúlveda, A.; Stesmans, A. Electrical characterization of ultrathin RF-sputtered LiPON layers for nanoscale batteries. *ACS Appl. Mater. Interfaces* **2016**, *8*, 7060–7069.

[49] Feng, W. L.; Hu, J. M.; Qian, G. N.; Xu, Z. M.; Zan, G. B.; Liu, Y. J.; Wang, F.; Wang, C. S.; Xia, Y. Y. Stabilization of garnet/Li interphase by diluting the electronic conductor. *Sci. Adv.* **2022**, *8*, eadd8972.

[50] Yu, Z. J.; Zhang, X. Y.; Fu, C. K.; Wang, H.; Chen, M.; Yin, G. P.; Huo, H.; Wang, J. J. Dendrites in solid-state batteries: Ion transport behavior, advanced characterization, and interface regulation. *Adv. Energy Mater.* **2021**, *11*, 2003250.

[51] Cui, C. Y.; Yang, C. Y.; Eidson, N.; Chen, J.; Han, F. D.; Chen, L.; Luo, C.; Wang, P. F.; Fan, X. L.; Wang, C. S. A highly reversible, dendrite-free lithium metal anode enabled by a lithium-fluoride-enriched interphase. *Adv. Mater.* **2020**, *32*, 1906427.

[52] Sastre, J.; Futscher, M. H.; Pompizi, L.; Aribia, A.; Priebe, A.; Overbeck, J.; Stiefel, M.; Tiwari, A. N.; Romanyuk, Y. E. Blocking lithium dendrite growth in solid-state batteries with an ultrathin amorphous Li-La-Zr-O solid electrolyte. *Commun. Mater.* **2021**, *2*, 76.

[53] Cao, D. X.; Sun, X.; Li, Q.; Natan, A.; Xiang, P. X.; Zhu, H. L. Lithium dendrite in all-solid-state batteries: Growth mechanisms, suppression strategies, and characterizations. *Matter* **2020**, *3*, 57–94.

[54] Jin, Y. M.; He, Q. S.; Liu, G. Z.; Gu, Z.; Wu, M.; Sun, T. Y.; Zhang, Z. H.; Huang, L. F.; Yao, X. Y. Fluorinated $Li_{10}GeP_2S_{12}$ enables stable all-solid-state lithium batteries. *Adv. Mater.* **2023**, *35*, 2211047.

[55] Fan, X. L.; Chen, L.; Borodin, O.; Ji, X.; Chen, J.; Hou, S.; Deng, T.; Zheng, J.; Yang, C. Y.; Liou, S. C. et al. Non-flammable electrolyte enables Li-metal batteries with aggressive cathode chemistries. *Nat. Nanotechnol.* **2018**, *13*, 715–722.

[56] Xu, H. H.; Li, Y. T.; Zhou, A. J.; Wu, N.; Xin, S.; Li, Z. Y.; Goodenough, J. B. Li_3N-modified garnet electrolyte for all-solid-state lithium metal batteries operated at 40 °C. *Nano Lett.* **2018**, *18*, 7414–7418.

[57] Yao, X. H.; Lu, X. K.; Zhou, Y. D.; Šamořil, T.; Bi, J. X.; Masteghin, M. G.; Zhang, H. X.; Askew, L.; Kim, J.; Xiong, F. Y. et al. Rectifying interphases for preventing Li dendrite propagation in solid-state electrolytes. *Energy Environ. Sci.* **2023**, *16*, 2167–2176.

[58] Tian, H. K.; Liu, Z.; Ji, Y. Z.; Chen, L. Q.; Qi, Y. Interfacial electronic properties dictate Li dendrite growth in solid electrolytes. *Chem. Mater.* **2019**, *31*, 7351–7359.

[59] Park, K.; Goodenough, J. B. Dendrite-suppressed lithium plating from a liquid electrolyte via wetting of Li_3N. *Adv. Energy Mater.* **2017**, *7*, 1700732.

[60] Raj, V.; Venturi, V.; Kankanallu, V. R.; Kuiri, B.; Viswanathan, V.; Aetukuri, N. P. B. Direct correlation between void formation and lithium dendrite growth in solid-state electrolytes with interlayers. *Nat. Mater.* **2022**, *21*, 1050–1056.

[61] Lewis, J. A.; Cortes, F. J. Q.; Liu, Y.; Miers, J. C.; Verma, A.; Vishnugopi, B. S.; Tippens, J.; Prakash, D.; Marchese, T. S.; Han, S. Y. et al. Linking void and interphase evolution to electrochemistry in solid-state batteries using *operando* X-ray tomography. *Nat. Mater.* **2021**, *20*, 503–510.

[62] Liang, Z. T.; Xiang, Y. X.; Wang, K. J.; Zhu, J. P.; Jin, Y. T.; Wang, H. C.; Zheng, B. Z.; Chen, Z. R.; Tao, M. M.; Liu, X. S. et al. Understanding the failure process of sulfide-based all-solid-state lithium batteries via *operando* nuclear magnetic resonance spectroscopy. *Nat. Commun.* **2023**, *14*, 259.

[63] Otoyama, M.; Suyama, M.; Hotehama, C.; Kowada, H.; Takeda, Y.; Ito, K.; Sakuda, A.; Tatsumisago, M.; Hayashi, A. Visualization and control of chemically induced crack formation in all-solid-state lithium-metal batteries with sulfide electrolyte. *ACS Appl. Mater. Interfaces* **2021**, *13*, 5000–5007.

[64] Ning, Z. Y.; Jolly, D. S.; Li, G. C.; De Meyere, R.; Pu, S. D.; Chen, Y.; Kasemchainan, J.; Ihli, J.; Gong, C.; Liu, B. Y. et al. Visualizing plating-induced cracking in lithium-anode solid-electrolyte cells. *Nat. Mater.* **2021**, *20*, 1121–1129.

[65] Kasemchainan, J.; Zekoll, S.; Spencer Jolly, D.; Ning, Z. Y.; Hartley, G. O.; Marrow, J.; Bruce, P. G. Critical stripping current leads to dendrite formation on plating in lithium anode solid electrolyte cells. *Nat. Mater.* **2019**, *18*, 1105–1111.

[66] Zhu, J. F.; Chen, J.; Luo, Y.; Sun, S. Q.; Qin, L. G.; Xu, H.; Zhang, P. G.; Zhang, W.; Tian, W. B.; Sun, Z. M. Lithiophilic metallic nitrides modified nickel foam by plasma for stable lithium metal anode. *Energy Storage Mater.* **2019**, *23*, 539–546.

[67] Yang, J.; Shang, J.; Liu, Q. R.; Yang, X. Y.; Tan, Y. F.; Zhao, Y.; Liu, C. G.; Tang, Y. B. Variant-localized high-concentration electrolyte without phase separation for low-temperature batteries. *Angew. Chem., Int. Ed.*, in press, DOI: 10.1002/anie.202406182.

[68] Zhang, Y. Q.; Gao, H. C.; Wang, J. S.; Chi, Q. G.; Zhang, T. D.; Zhang, C. H.; Feng, Y.; Zhang, Y.; Cao, D. X.; Zhu, K. PEO/$Li_{1.25}A_{l0.25}Zr_{1.75}(PO_4)_3$ composite solid electrolytes for high-rate and ultra-stable all-solid-state lithium metal batteries with impregnated cathode modification. *Inorg. Chem. Front.* **2024**, *11*, 1289–1300.

[69] Swamy, T.; Chen, X. W.; Chiang, Y. M. Electrochemical redox behavior of Li ion conducting sulfide solid electrolytes. *Chem. Mater.* **2019**, *31*, 707–713.

[70] Taklu, B. W.; Su, W. N.; Nikodimos, Y.; Lakshmanan, K.; Temesgen, N. T.; Lin, P. X.; Jiang, S. K.; Huang, C. J.; Wang, D. Y.; Sheu, H. S. et al. Dual CuCl doped argyrodite superconductor to boost the interfacial compatibility and air stability for all solid-state lithium metal batteries. *Nano Energy* **2021**, *90*, 106542.

[71] Wang, Y. Q.; Lü, X. J.; Zheng, C.; Liu, X.; Chen, Z. H.; Yang, W. G.; Lin, J. H.; Huang, F. Q. Chemistry design towards a stable sulfide-based superionic conductor $Li_4Cu_8Ge_3S_{12}$. *Angew. Chem., Int. Ed.* **2019**, *58*, 7673–7677.

[72] Xu, R. C.; Han, F. D.; Ji, X.; Fan, X. L.; Tu, J. P.; Wang, C. S. Interface engineering of sulfide electrolytes for all-solid-state lithium batteries. *Nano Energy* **2018**, *53*, 958–966.

[73] Zhao, F. P.; Alahakoon, S. H.; Adair, K.; Zhang, S. M.; Xia, W.; Li, W. H.; Yu, C.; Feng, R. F.; Hu, Y. F.; Liang, J. W. et al. An air-stable and Li-metal-compatible glass-ceramic electrolyte enabling high-performance all-solid-state Li metal batteries. *Adv. Mater.* **2021**, *33*, 2006577.

[74] Zhao, F. P.; Liang, J. W.; Yu, C.; Sun, Q.; Li, X. N.; Adair, K.; Wang, C. H.; Zhao, Y.; Zhang, S. M.; Li, W. H. et al. A versatile Sn-substituted argyrodite sulfide electrolyte for all-solid-state Li metal batteries. *Adv. Energy Mater.* **2020**, *10*, 1903422.

[75] Liu, Y.; Su, H.; Zhong, Y.; Wang, X. L.; Xia, X. H.; Gu, C. D.; Tu, J. P. Revealing the impact of Cl substitution on the crystallization behavior and interfacial stability of superionic lithium argyrodites. *Adv. Funct. Mater.* **2022**, *32*, 2207978.